Chapter 5

Analysis of combined dataset

In this Chapter we perform the search for dark matter decay lines in X-rays at energies 2.8 – 10.8 keV, by stacking the X-ray spectra of *nearby spiral and dwarf galaxies* observed with *XMM-Newton*. To this end we collect several hundreds observations of nearby galaxies. After careful data reduction (removing point sources, time variable component and other sources of contamination) we end up with the dataset of about 400 observations with the total *cleaned* (usable) exposure of about 6 Msec (about two orders of magnitude longer than any single observation with *XMM-Newton*). Large number of counts in each energy bin corresponds to the *statistical error* at the sub-per cent level. We build a spectrum of the combined dataset and demonstrate that we are able to describe it with a simple, physically motivated model, so that all the remaining residuals (i.e. systematic errors) remain at a comparable (sub-per cent) level. Careful analysis of this dataset reveals a number of line-like residuals at the level $2-3\sigma$. We investigate each of these candidates and demonstrate that none of them can be interpreted as an astrophysical line, originating from dark matter decays. The resulting limits on the flux in lines are at the level of about several $\times 10^{-6}\mathrm{photons/sec/cm}^2$ (apart from the bins where strong instrumental lines are present), which constitute as much as an order of magnitude improvement compared to the existing bounds.

The rest of this Chapter is organized as follows. We discuss the choice of targets in Sections 5.1. Our data reduction technique is presented in Section 5.2. Section 5.3 is devoted to the description of the stacked spectrum of all galaxies. Section 5.3.1 describes in details our approach to modeling the spectrum. Finally, in Section 5.5 we discuss our results: detected weak lines,

their possible origin and resulting bounds on the line flux.

5.1 Selecting objects for the combined dataset

Using the archive of X-ray observations of the *XMM-Newton*, it is possible to collect about 20 Msec of the nearby spiral and irregular galaxies[1]. The choice of the objects was dictated by several considerations:

- the absence of too many bright point sources. Indeed, removal of each point source leads to the decrease of the field-of-view and of dark matter decay signal (proportional to the FoV) by about 0.5%.[2] Therefore, for the large amount of removed point sources the expected signal to noise starts to decrease (see e.g. the analysis of [230]).
- the absence of prominent diffuse emission at energies of interest. This requirement restricted our attention to galaxies, whose diffuse emission is concentrated in soft X-ray band (below $\sim 2\,\mathrm{keV}$), thus discarding not only observations of clusters, but also of giant elliptical galaxies.
- angular size of the object should be sufficiently large to cover the FoV of the *XMM-Newton* EPIC camera ($\sim 26'$ in diameter). If the solid angle spanned by the characteristic size of dark matter distribution r_* is much bigger than the FoV of the satellite, the uncertainty of exact modeling of dark matter distribution at the centers of galaxies become significant. If, on the other hand, the characteristic scale is much smaller than the FoV, one looses the signal (which scales as $\Omega_{\rm fov}\times\bar{\mathcal{S}}$, see Eq. (3.3)). Therefore, optimal objects are those whose characteristic radius of dark matter distribution is of the order of the radius of the FoV – the nearby galaxies.

We saw in Chapter 3 that the dark matter column density in of the Milky Way halo is comparable to the signal from other objects (see also [223, 228, 231, 367]). Therefore we start with collecting *recent* results on the Milky Way dark matter distributions and analyzing the uncertainties of the corresponding column density estimates. We then continue with identifying the galaxies, whose expected decay signal would be comparable (constitute a sizable fraction) of the Milky Way's contribution in their direction. Section 5.1.5 summarizes our dataset.

[1] We do not consider galaxy clusters, as their strong X-ray background would require a different type of analysis.

[2] The point spread function of the *XMM-Newton* (encircled 90% of photon energy) is 40-60 arcsec and we remove circle with the radius $1'$ around each point source.

Reference	Type	$\rho_s(\rho_c)$, $10^6 M_\odot/\ \mathrm{kpc}^3$	$r_s(r_c)$, kpc	$r_\odot$, kpc
[194]	NFW	4.9	21.5	8.0
[194][a]	NFW	0.60	46.1	8.5
[370]	NFW	13.3	14.7±0.7	8.0
[371]	NFW	27.2±15.0	10.2±6.1	7.5
[372][b]	NFW	4.74±0.57	21.0±3.2	8.0
[373]	ISO	24.5±2.5	5.5±0.6	8.0
[374]	NFW	20.4±2.6	10.8±3.4	8.33±0.35
[375]	NFW	12.5±6.0	17.0±3.9	8.33±0.35

Table 5.1: Parameters of dark matter profiles for Milky Way galaxy. Here, ρ_s (ρ_c) and r_s (r_c) denote the characteristic density and radius of the NFW (ISO) dark matter distributions, see Eq. 3.8 and Eq. 3.11, respectively, $r_\odot$ is the distance to Galactic Centre.

[a] Maximum disk profile.

[b] Mass-concentration relation between distribution parameters is assumed.

5.1.1 Milky Way galaxy

The mass modeling of the Milky Way is continuously updated and improved (see e.g. [194, 195, 368–375]). In Table 5.1 we summarize recent results. For each of the profiles the dark matter column density is calculated using the expression (3.5). The results are shown in Fig. 5.1. The behaviour of cored (ISO) and cusped (NFW) profiles differs at small ϕ. Notice that the difference becomes much less profound if the column density is averaged over the field of view of *XMM-Newton* (radius $15'$). In what follows we only consider observations with the off-center angle $\phi \gtrsim 45^\circ$.

As we see from Fig. 5.1, *the most conservative values of dark matter column density in this region of ϕ is given by the NFW profile from [372].* For comparison, we also show in Fig. 5.1 the most "extreme" case of Milky Way mass modeling — the maximal disk distribution of [194].[3] This model is highly implausible, in particular because the maximal disk would be unstable (see [194] for discussion). We do not use this profile in our calculations and keep it to demonstrate the level of uncertainties.

[3] In calculating the dark matter column density for this profile we did not take into account additional effect of adiabatic contraction, so the actual signal is stronger in the center.

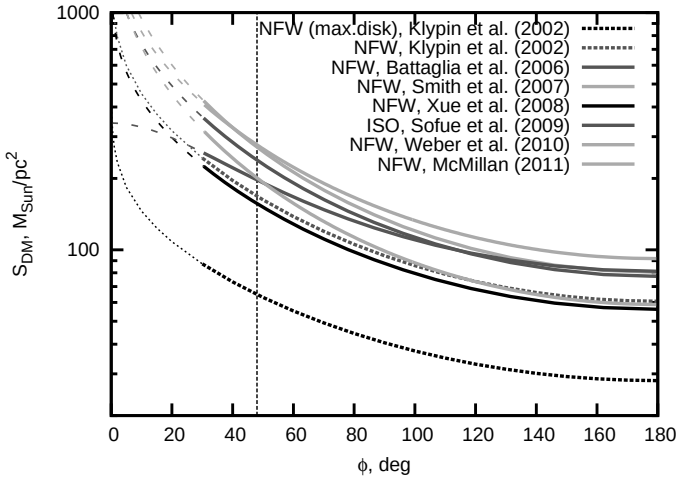

Figure 5.1: Comparison of different dark matter column density distributions of the Milky Way halo as a function of the off-centre angle ϕ (see Eq. (3.6) for its definition). All observations in our combined dataset have the angle $\phi > 48^\circ$ (to the right of vertical line). We adopt profile "NFW, Xue et al. (2008)" [372] as the most conservative column density estimate. We also show (in black dotted line) the most extreme case – the maximal disk profile from [194]. This model is unphysical, designed solely to minimize the dark matter content, and is only showed for demonstrate the level of uncertainties, which is less than a factor of 2 even in this case.

5.1.2 Galaxies of the Local Group

Among all objects that we choose for the combined dataset, there are three objects that are parts of the Local group: Large and Small Magellanic Clouds and the Andromeda galaxy. These objects are special in a number of ways. First of all, their dark matter halos have size about several degrees – much larger than the *XMM-Newton* field-of-view. Therefore, if a candidate line is found, its surface brightness in these objects can be studied. Secondly, large X-ray surveys had covered significant fractions of these galaxies [376–378]. Finally, as we are going to see, these objects have dark matter column density similar (or greater) than the Milky Way's contribution in this direction, thus significantly increasing the expected signal.

Reference	Type	$\rho_s(\rho_c)$, $10^6 M_\odot/\,\mathrm{kpc}^3$	$r_s(r_c)$ kpc
[285]	NFW	37.0	8.18
[285]	NFW	47.1	7.63
[285][a]	NFW	2.11	28.73
[298]	BURK	57.2	6.86
[298]	NFW	17.4	12.5
[11][b]	BURK	2.915	28
[11][c]	NFW	4.81	22.952

Table 5.2: Parameters of dark matter profiles for M31 used in this Chapter.
[a] Maximum disk profile.
[b] Mass-radius relation between distribution parameters is assumed.
[c] Mass-concentration relation between distribution parameters is assumed.

5.1.2.1 Andromeda galaxy

The dark matter distributions for the Andromeda galaxy was extensively discussed in Sec. 4.1.3.1. We reproduce it here, adding several new profiles and discarding the dark matter distributions from [12] because of bad quality of fit. The results and their uncertainties are summarized in Table 5.2. We adopted the distance to M31 $D_{\mathrm{M31}} = 785\ \mathrm{kpc}$ [379]. Dark matter column density profiles as a function of the off-center angle within Andromeda halo are shown in Fig. 5.2. The BURK profile from [11] is used as the most conservative one, similarly to Sec. 4.1.3.1.

5.1.2.2 Large and Small Magellanic Clouds

For LMC, we used the dark matter density distribution parameters from [380–382], see Table 5.3 for details. The results for dark matter column density are shown in Fig. 5.3.

For SMC, we used the dark matter density distribution parameters from [384], see Table 5.4 for details. The results for dark matter column density are shown in Fig. 5.4.

Our analysis shows that both LMC and SMC dark matter content is highly uncertain. Therefore, while it is natural to expect a significant boost of a signal (and thus include these objects as a part of the dataset), in deriving conservative bounds, one has to assume negligibly small content of

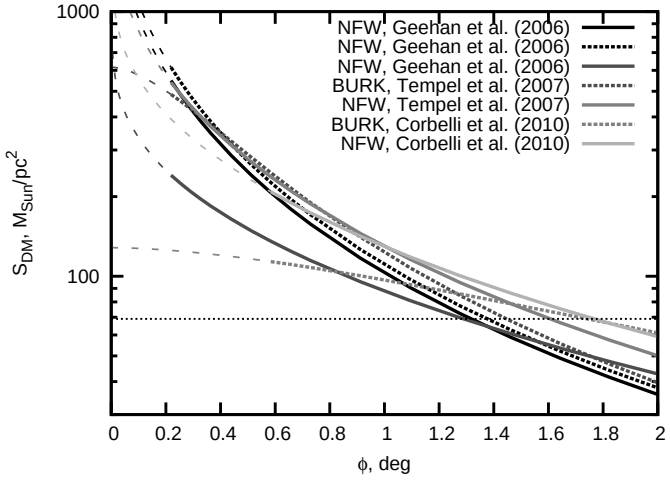

Figure 5.2: Dark matter column density in the Andromeda galaxy, based on the different dark matter distributions, described in Table 5.2. The BURK profile from [11] is the 'minimal' dark matter model used in [323], see also Sec. 4.1.3.1 for details. Here, we adopt this profile as the most conservative estimate. Horizontal line shows the minimal contribution from the Milky Way halo in direction of M31, the most conservative profile from [372], see Fig. 5.1 for details.

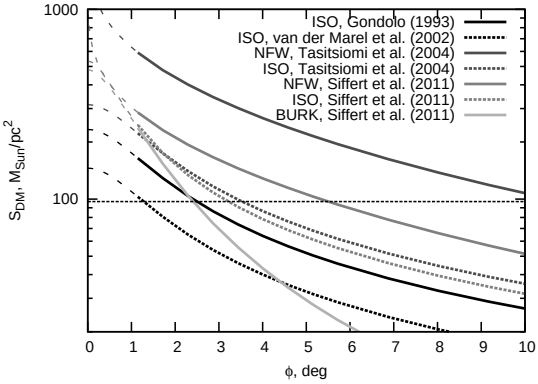

Figure 5.3: Comparison of different dark matter column density distributions of the Large Magellanic Cloud. The parameters of these profiles are described in Table 5.3. Horizontal line shows the minimal contribution from Milky Way halo in the direction of LMC, using the most conservative profiles from [372], see Fig. 5.1 for details.

Reference	Type	$\rho_s(\rho_c)$, $10^6 M_\odot/\,\mathrm{kpc}^3$	$r_s(r_c)$ kpc
[380][a]	ISO	74	1
[383]	ISO	46.3	1
[381][b]	NFW	16.6	9.16
[381]	ISO	100	1
[382]	NFW	8.18±2.67	9.04±2.43
[382][c]	ISO	326±65	0.52±0.076
[382][c]	BURK	289±51	1.06±0.13

Table 5.3: Parameters of dark matter profiles for LMC.
[a] Halo radius is uncertain $\lesssim 10$ kpc, only combination $\rho_c r_c^2$ is measured.
[b] Minimal disk assumption.
[c] Bad quality of fit.

Reference	Type	$\rho_s(\rho_c)$, $10^6 M_\odot/\,\mathrm{kpc}^3$	$r_s(r_c)$ kpc
[384][a]	NFW	4.1	5.1
[384][b]	BURK	21.4	3.2

Table 5.4: Parameters of dark matter profiles for SMC used in this Chapter.
[a] Bad quality of fit.
[b] Best-fit relation between distribution parameters is assumed.

dark matter, using only Milky Way's column density in the direction of these objects.

5.1.3 Galaxies with measured dark matter distribution

We collect the dark matter distributions of galaxies, using the catalogue compiled in Chapter 3. We derive the *average* dark matter column density inside a circle with radius $15'$, corresponding to the FoV radius for *XMM-Newton* imaging spectrometers. To be conservative, we use *truncation of cuspy profiles* (NFW). Namely for $r > r_s$ the average dark matter column density coincides with the NFW expression while for $r \leq r_s$ it remains *constant* (similar to cored profiles).

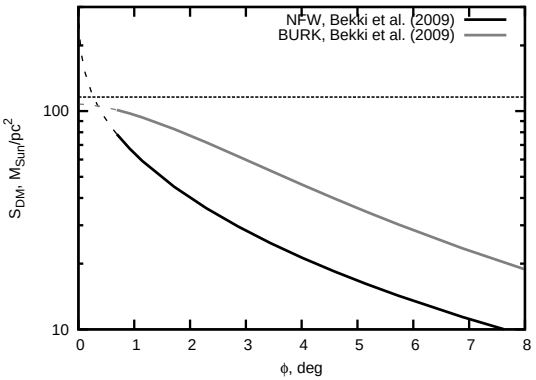

Figure 5.4: Comparison of different dark matter column density distributions for the Small Magellanic Cloud. The parameters of these profiles are described in Table 5.4. Horizontal line shows the minimal contribution from the Milky Way halo in the direction of SMC, using the most conservative profile from [372], see Fig. 5.1 for details.

5.1.4 Galaxies with unknown matter distribution

Apart of galaxies with known dark matter distributions, for a large number of nearby galaxies that fall within the FoV of *XMM-Newton* do not have available data for dark matter density profiles. To *estimate* the dark matter distribution parameters for these galaxies, we used the following procedure.

We took the values of galaxy optical radius r_{opt} obtained from the apparent angular diameter, `logdc` (corrected for the galactic extinction and inclination effect) from the `HyperLeda` database.[4] The distance to the galaxy was also obtained from HyperLeda database either from "true" distance modulus `mod0` (when available) or from redshift distance modulus `modz` for sufficiently distant galaxies (with $cz \geq 200$ km/s). This results in more than $5{\times}10^4$ galaxies with known `logdc` values.

Then, using the sample of 92 spiral and elliptical galaxies from our catalogue, complied in Chapter 3, we study log-log correlations of r_{opt} with r_* and $\mathcal{S} \propto \rho_* r_*$.[5] The best-fit parameters of the correlations (see also Fig. 5.5 for

[4] `http://leda.univ-lyon1.fr`

[5] Recall that the parameters ρ_* and r_* coincide with the parameters ρ_s and r_s correspondingly for the NFW distribution. For other distributions, see Section 3.12 for details.

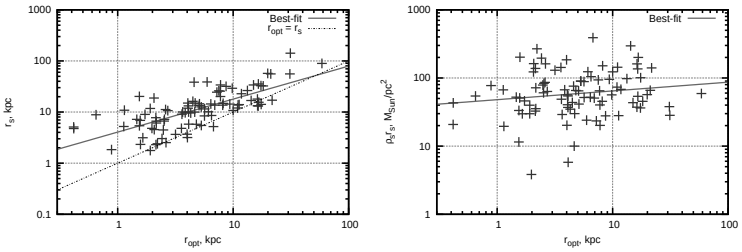

Figure 5.5: *Left:* Correlation between the optical radius r_{opt} defined with the help of HyperLeda database and characteristic size of galactic dark matter haloes r_* compiled from dark matter catalogue of Chapter 3. The best-fit values are presented in Eq. 5.1. Note that for most of the objects $r_* > r_{opt}$, in agreement with expectations. *Right:* The same correlation but with $\rho_* r_*$, a proxy for dark matter column density $\mathcal{S}$.

details) are:

$$\log_{10}\left(\frac{r_*}{1\,\mathrm{kpc}}\right) = 0.646 \times \log_{10}\left(\frac{r_{opt}}{1\,\mathrm{kpc}}\right) + 0.607;$$
$$\log_{10}\left(\frac{\rho_* r_*}{1 M_\odot/\,\mathrm{pc}^2}\right) = 0.129 \times \log_{10}\left(\frac{r_{opt}}{1\,\mathrm{kpc}}\right) + 1.68. \qquad (5.1)$$

Finally, the correlations Eq. (5.1) are then used to determine the parameters of dark matter density distributions for about 5×10^4 galaxies not present in our dark matter distribution catalogue. Namely, we choose such objects for which angular size of $r_* \gtrsim 15'$ and then estimate its column density. We sub-select only those galaxies that have estimate $\mathcal{S} \geq 30 M_\odot\,\mathrm{pc}^{-2}$.

5.1.5 Combined dataset: summary

All together our procedures, outlined in Sections 5.1.1–5.1.4 resulted in the sample of **111** galaxies, see [385] for details. By using HEASARC browsing form [386], we selected all of them observed by *XMM-Newton* with a pointing centered inside a circle with the radius $r_*/D + 15'$ from the centre of a given galaxy. Such a selection finds observations covered the innermost part of the dark matter halo of the object. This results in 70 galaxies observed by *XMM-Newton*. 61 of them are included in our final dataset, see [387] for details.

Total *uncleaned XMM-Newton* exposure of these galaxies is $\sim$ 19 Ms.

About 50% of this exposure is concentrated on three galaxies with the largest angular size of the dark matter halo – Large Magellanic Cloud (LMC), Small Magellanic Cloud (SMC) and Andromeda galaxy (M31).

5.2 Data processing

5.2.1 Downloading and preprocessing *XMM-Newton* data

We use the data obtained with the European Photon Imaging Camera (EPIC) of *XMM-Newton*, which consists of two MOS [388] and one PN [389] CCD cameras (sensitive in the 0.1-15 keV energy range) behind X-ray telescopes [390]. We download the basic Observation Data Files (ODF) for 725 publicly available (on April 16 2012) *XMM-Newton* observations for 70 galaxies selected in previous Sec. 5.1 using the web search form of NASA's High Energy Astrophysics Science Archive Research Center (HEASARC) [386]. In accordance with startard data analysis prescription, see e.g. Sec. 4.3 of [391], we produced *calibrated concatenated event*[6] *lists* using the standard data reduction procedures[7] `emproc` and `epproc` for MOS [388] and PN [389] cameras of *XMM-Newton*/EPIC, respectively. These procedures include combining data from all CCDs for each camera (MOS1, MOS2, PN), identification and rejection of bad CCD pixels, calculation of event coordinates using telescope attitude information and improving the quality of PN data at low energies.

The filtered event lists are then used for timing and spatial variability filtering described in the next Sec. 5.2.2 and Sec. 5.2.3. The main statistical properties event lists before and after the cleaning procedure are given in Table 5.5. The detailed parameters of the *filtered* event lists are presented in [387].

[6]Here, an "event" is a result of instantaneous positive detection in one or several adjacent CCD pixels. According to Sec.4.4 of [391], storing detector data in format of events is motivated by telemetry contraints of the *XMM-Newton* satellite. Indeed, according to [334] the procedure based on analysis of event patterns allows to reject of about 99% of events caused by high-energy (~ 100 MeV) cosmic rays thus significantly reducing the amount of data telemetry.

[7]These procedures are the part of the standard publicly available software of *XMM-Newton* data analysis, Science Analysis System (SAS) v.11.0.0 [392].

5.2.2 Removing time-variable component

Raw event lists, generated using the standard pipeline (see Sec. 5.2.1 for description), exhibits significant time variability, both in short ($\lesssim$ 10 ks) and long ($\gtrsim$ 10 ks) scale variability. According to [325], the short-scale time variability is caused by the soft solar protons with the energies about few 100 keV. The countrate spectrum of these *soft proton flares* has unpredictable shape although it can be approximated by broken powerlaw with $E_{break} \simeq 3.2$ keV [329]. Moreover, according to our findings in Sec. 4.1.5 (see also [323]), residual soft proton flare contamination is also responsible for (at least) the broad line-line feature at 2.5-2.6 keV, where the effective area has a local minimum due to Au K edge. The count rate of the decaying dark matter signal should be of course constant in time and therefore we aim to clean the time variability as much as possible.

A number of different methods of removing time-variable component has been developed (Appendix 8.4.1 provides a brief overview of available procedures). Here we apply the following procedure. First, by using the 60 s histogram for the whole energy range (0.2–12 keV for MOS and 0.15–15 keV for PN camera) we reject the countrates differing from the mean value at more than 1.5σ. This is done with the help of standard procedure `espfilt` [393]. This procedure removed 34%, 33% and 43% of total observation time for MOS1, MOS2 and PN cameras, respectively (see Table 5.5 for details). The subsequent visual inspection of cleaned lightcurves showed the absence of any significant time variability. To further clean the residual soft proton component, we apply the procedure of [330]. It is based on comparison of high-energy (6-12 keV for MOS, 5–7.3 and 10–14 keV for PN) countrates for "in-FoV" (10-15 arcmin off-center) and out-FoV CCD regions, using their public script [331][8]. Fig. 5.6 shows the obtained dependence on $F_{in} - F_{out}$ ratios from F_{in} in MOS and PN cameras. In accordance with [330], we selected observations with $F_{in} - F_{out}$ less than 1.50 (marked by horisontal line). In addition, we removed observations with $F_{in} \geq 0.35$ cts/s for MOS and 1.2 cts/s for PN camera (marked by vertical lines in Fig. 5.6) which show significant large-scale variability at high energies.

The final step of removing large-scale time variability is made after re-

[8]This script does not take into account the damage of MOS1 CCD6 on 09 March, 2005, see [394, 395] for details. According to [331], the relative error on MOS1 $F_{in} - F_{out}$ ratio after the damage is about 10 %.

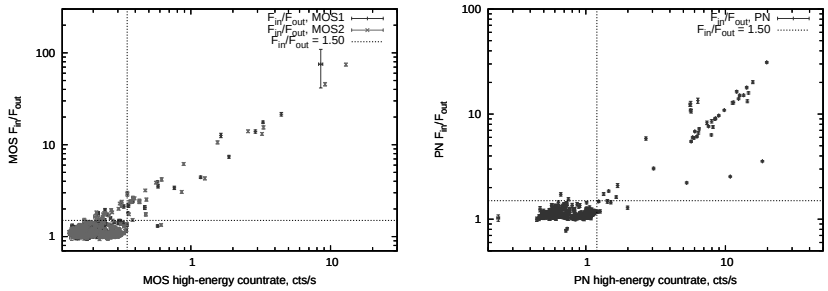

Figure 5.6: F_{in}/F_{out} for MOS (*left*) and PN (*right*) cleaned event lists as functions of F_{in}. The adopted selection criteria on $F_{in}/F_{out} \leq 1.30$ proposed by [330] are also shown. Additionally, we select observations having $F_{in} \leq 0.35$ cts/s for MOS and $F_{in} \leq 1.2$ cts/s for PN camera, shown by horizontal lines.

moving observations with significant changes of instrumental background flux [325, 352]. As a result, our filtering leaves 359 MOS1, 327 MOS2 and 321 PN cleaned event lists, see Tables 5.5 and [387] for details.

The mean value of $F_{in} - F_{out}$ ratio for our dataset is 1.13 ± 0.11 for MOS1, 1.10 ± 0.10 for MOS2 and 1.12 ± 0.10 for PN camera, see Table 5.5 for details. The histogram of observations basen on their $F_{in} - F_{out}$ ratios is shown in Fig. 5.7.

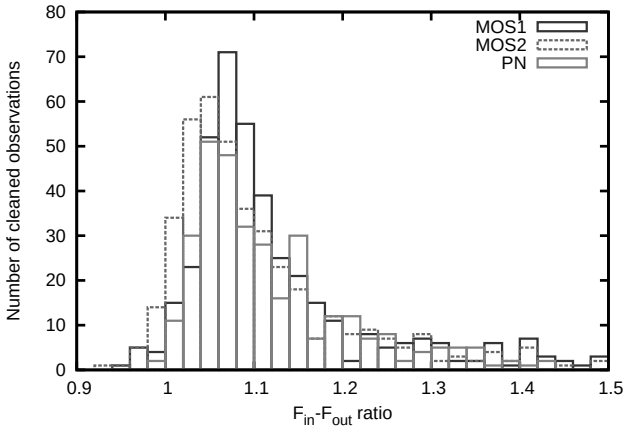

Figure 5.7: Histogram of the distribution of MOS1, MOS2 and PN observations as function of their $F_{in} - F_{out}$ ratio for dataset.

5.2.3 Filtering spatial variability.

Presence of spatial variability may significantly affect our results due to narrow emission lines from astrophysical sources. Indeed, as we see from left Fig. 5.8, the 2.5-6.0 keV brightness (flux per unit solid angle) *before* filtering spatial variability is about 4-72 (MOS) and 10-180 (PN camera). This is much larger compared to typical values for blank-sky dataset [327] (excluding Galactic Centre region): 5-10 (MOS) and 30-48 (PN camera). Therefore, additional cleaning of spatial variability should be performed.

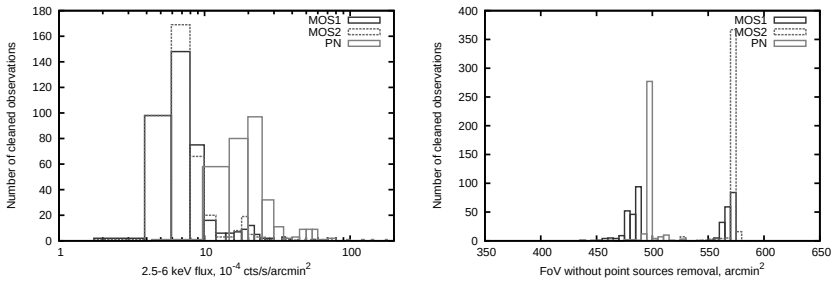

Figure 5.8: *Left*: histogram of the distribution of MOS1, MOS2 and PN observations as function of their 2.5-6.0 keV flux *before* spatial variability cleaning. These values are considerably larger than the typical values for blank-sky spectra, about 5-10$\times 10^{-4}$ cts/(s arcmin^2) for MOS and 30-48$\times 10^{-4}$ cts/(s arcmin^2) for PN camera (excluding Galactic Centre region), according to Table 3 of [327], so additional cleaning for spatial variability should be performed. *Right*: histogram of the distribution of MOS1, MOS2 and PN observations as function of the size of their field-of-view.

In the literature, we identifed the following sources of spatial variability:

1. Bright strips in PN camera caused by out-of-time events (see Sec.4.10 of [391]);
2. Anomalous CCD states [329, 353];
3. Point and extended astrophysical sources.

The *out-of-time events* are caused by photons coming during the CCD readout phase, see Sec. 4.10 of [391] for details. During the readout time, these events assign the wrong number of a detector coordinate RAWY and thus wrong energy correction value. As a result, out-of-time events form bright strips in images parallel to CCD borders. The fraction of out-of-time

events depends on observation mode according to Sec. 3.3.10 of [320], it is the largest for Full Frame (6.3 %) and Extended Full Frame (2.3 %) modes for PN camera. For these modes, we correct PN spectra with the standard procedure [324] by creating the simulated out-of-time event list, producing its properly scaled spectrum (using the same detector coordinates as in the source file) and subtracting it from the source spectrum.

Anomalous CCD state appears for some observations, where the countrate for some CCDs is significantly larger than for nearby CCDs. According to [329, 353], the anomalous states significantly affect the CCD countrate for $E \lesssim 1.0$ keV. Because here we concentrate on $\gtrsim 2.8$ keV energy range, we do not exclude the corresponding CCDs from the subsequent analysis.

Due to instrument diffraction and mirror defects, *astrophysical point sources* appear to have finite size. It is determined by the *point spread function* (PSF) [9] and is usually about several tens of arcsecs, much larger than the size of a CCD pixel. This allows to detect the point source by comparing the countrate in several adjacent pixels with that of background. However, this algorithmical procedure is complicated by the precence of CCD gaps, bad pixels, spatial vignetting[10]. We identified point astrophysical sources using standard *XMM-Newton* SAS metatask `edetect_chain` [396]. To increase the sensivitity with respect to point source detection, we used simultaneously MOS and PN cameras. We excluded all point sources detected in a circle with 14 arcmin radius[11] at $\gtrsim 4\sigma$ level together with 60-arcsec circular regions centered at the their positions. According to Sec. 3.2.1 of [320], such circle contains more than 90 % of source energy up to off-axis angle of 10 arcmin (MOS) or up to 3 arcmin (PN camera). Subsequent visual inspection has not found significant remaining point sources.

To check for *extended astrophysical sources*, we first calculated 2.5-6 keV brightness and compared it with *blank-sky* dataset of [327]. The solid angle covered by field-of-view is calculated with standard `backscale` procedure [397]. Before point source subtraction, the field-of-view solid angles are distributed according to right Fig. 5.8. Notably, all of them are somewhat smal-

[9] For the shapes and extents of the MOS and PN point spread functions, see Sec. 3.2.1 of [320].

[10] Due to vignetting effect, the off-axis effective area of a telescope significantly (up to 2-3 times) decreases with increase of off-axis angle. This effect also strongly depends on energy, see Sec. 3.2.2 of [320] for details.

[11] This is somewhat smaller than the radius *XMM-Newton* field-of-view ($\simeq$ 15 arcmin) due to slightly different geometries of MOS and PN cameras.

ler than the naive estimate for a solid angle of a circle with 14 arcmin radius ($\pi \times 14^2 = 616$ arcmin^2) due to

- CCD gaps;
- bad pixels;
- loss of MOS1 CCD6 since 09 March, 2005, see [394] for details.

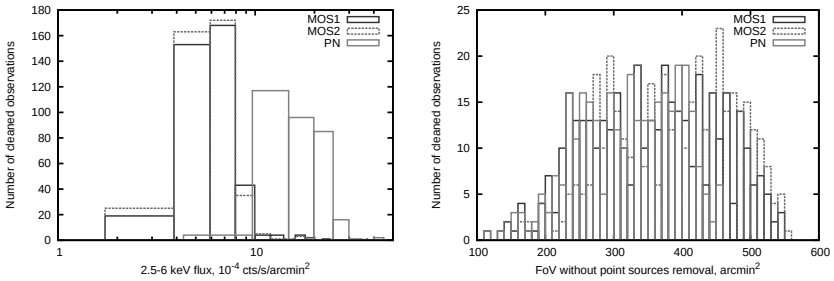

Figure 5.9: *Left*: histogram of the distribution of MOS1, MOS2 and PN observations as function of their 2.5-6.0 keV brightness *after* spatial variability cleaning. The results are close to typical values for blank-sky spectra, about 5-10$\times 10^{-4}$ cts/(s arcmin^2) for MOS and 30-48$\times 10^{-4}$ cts/(s arcmin^2) for PN camera (excluding Galactic Centre region), according to Table 3 of [327]. *Right*: histogram of the distribution of MOS1, MOS2 and PN observations as function of their field-of-view *after* spatial variability cleaning.

The distribution of X-ray brightness in 2.5-6 keV *after* subtraction of point sources becomes consistent with expectations from blank-sky dataset of [327], see left Fig. 5.9. However, by looking at temporal variations of X-ray brightness, see Fig. 5.10 it is possible to select several dozens of clear "outliers".

5.2.4 Producing raw spectra and response files

Event lists filtered from time and spatial variability (see previous Sections 5.2.2 and 5.2.3 for detailed description of cleaning procedure) are then used to produce spectra of individual observations. In an event list, each event contains information about *Pulse Height Invariant* (PI) – corrected and recombined (for non-single events) event energy. The standard procedure `evselect` [398] creates a histogram of events using their PI values in a

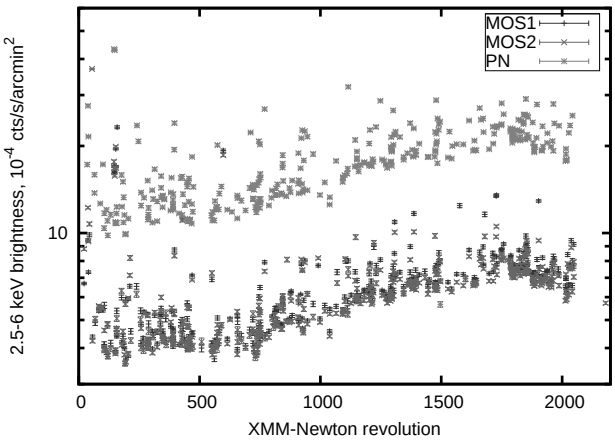

Figure 5.10: Temporal variation of X-ray brightness after subtraction of point sources (see Fig. 5.9), as a function of *XMM-Newton* revolution number. The errors are at 1σ level. Unlike Fig. 5.9, a number of "outlier" observations is clearly visible. For subseuqent analysis, we remove all these outlier observations.

pre-defined energy range with given binning interval. We use default values for energy ranges and binning intervals recommended by *XMM-Newton* SAS team. Namely, MOS spectra are binned by 15 eV in interval 0-11999 eV, PN spectra – by 5 eV in interval 0-20479 eV. This gives 800 energy channels for MOS and 4096 channels for PN camera.

In general, the difference between PI energy and actual photon energy includes the following effects:

1. Quasi-gaussian broadening of a narrow energy line with full width at half-maximum (FWHM) $\sim$100-200 eV, see e.g. Sec. 3.3.4 of [391];

2. Low-energy tail probably caused by incomplete charge collection for X-rays absorbed near CCD surface layer, see e.g. [399, 400].

3. Si fluoresence (at 1.740 keV) and Si escape (at $E - 1.740$ keV) peaks for input energies larger than the Si K edge at 1.839 keV, see [389, 401] for details. The intensity of Si escape peak may be at the order of several % of the main peak [402].

To model these effects, the *redistribution matrix file (RMF)* should be created. It contains the probability of the photon with *physical* energy between

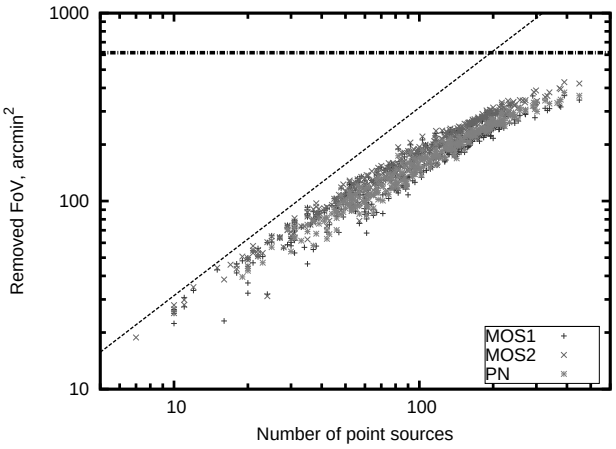

Figure 5.11: Part of the FoV, removed with point sources, as a function of the number of detected sources. Horizontal dashed-dotted line shows the full FoV of EPIC camera (circle with the radius of $13'$). Dashed line shows the upper bound of removed FoV fraction ($3.14\,\mathrm{arcmin}^2$ per source, provided that the $1'$ circles around sources do not overlap and there are no CCD gaps, bad pixels, etc.). As expected, for large number of removed sources, 1 arcmin circles around them overlap.

E and $E+\Delta$, where Δ is the size of the energy bin to be detected in spectral bin I. According for stardard prestrictions for analysis of extended sources, we simulated RMF files for each observation and camera (MOS1, MOS2, PN) using the standard *XMM-Newton* SAS task `rmfgen` [403] taking into account spatial distribution of the photons.

Then, to convert the obtained countrates (in cts/s) to fluxes (in cts/s/cm^2) we simulated files containing information about the effective area (ancillary response function, ARF) taking into account

1. Spatial distribution (to correct for PSF and telescope vignetting);
2. Quantum efficiency of the CCDs;
3. Presence of bad pixels;
4. Filter transmission efficiency [12];

[12]To attenuate the large photon countrates at low energies ($\lesssim 1$ keV), several filters (Thin, Medium, Thick) are used. According to Sec. 3.3.6 of [320] the difference between the effective area for different filters is $\lesssim 10\%$ for $E \gtrsim 2$ keV, so we do not make any differences between

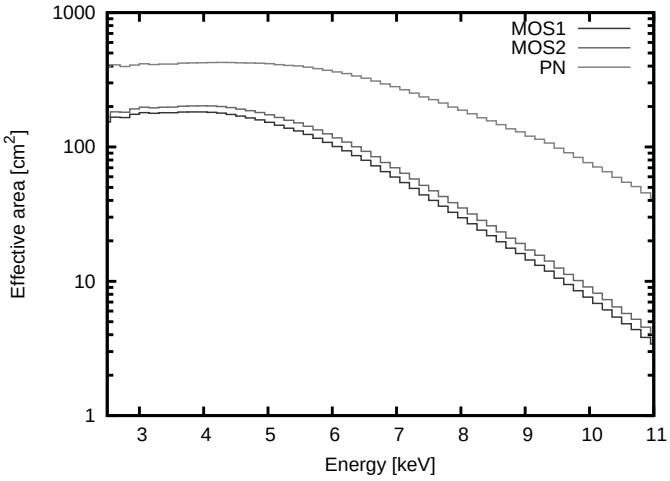

Figure 5.12: Exposure and FoV-weighted mean effective area for MOS1, MOS2 and PN cameras, as functions of energy. Note much larger effective area for PN camera at $E \gtrsim 5$ keV, compared to that of MOS cameras.

5. Correction for Out-of-time events (significant for PN Full Frame and Extended Full Frame observation modes).

Similar to RMF generation, we simulate ARF files for each observation and camera using the standard *XMM-Newton* SAS task `arfgen` [404].

The obtained spectra, together with RMF and ARF files, will be used for further modeling. The first step is to prepare combined spectrum of all observations for each of *XMM-Newton*/EPIC cameras (MOS1, MOS2, PN). Because the default size of binning intervals is much smaller than the energy resolution of the instrument, it lead this leads to significant oversampling of the data because the adjacent spectral bins are strongly correlated with each other. Therefore, we *rebin* the combined spectra into the larger bins. The size of the bin is a trade-off between oversampling (which is better with increasing the size of the bin) and better knowledge of the spectral line shape (which tends to decrease the size of the bin). As a result, we selected the size of the bin to be 60 eV for both MOS and PN cameras. The resulting spectra are shown in Fig. 5.13.

the observations with different filters.

	MOS1	MOS2	PN
Cleaned event lists	715	719	664
Raw exposure, ks	18756	19762	15908
Cleaned exposure, ks	12326	13193	9020
Fraction of exposure, affected by flares	34%	33%	43%
Small FoV cleaned event lists	175	167	138
Small FoV exposure, ks	2209	2374	1883
Short (< 5 ks) observations	113	104	154
Total exposure of short observations, ks	273	254	338
Full FoV Cleaned event lists	427	448	372
Full FoV exposure, ks	9844	10565	6799
Average $F_{in} - F_{out}$ of final dataset	1.13 ± 0.11	1.10 ± 0.10	1.12 ± 0.10
Average FoV before point sources removal, arcmin^2	518.0	566.4	498.4
Average FoV after point sources removal, arcmin^2	374.3	404.5	347.0
Number of event lists in the final dataset	359	327	321
Exposure of the final dataset, ks	8740	8241	5800

Table 5.5: Statistical properites of the combined dataset during the main stages of our analysis. See [387] for the basic properties of selected observations.

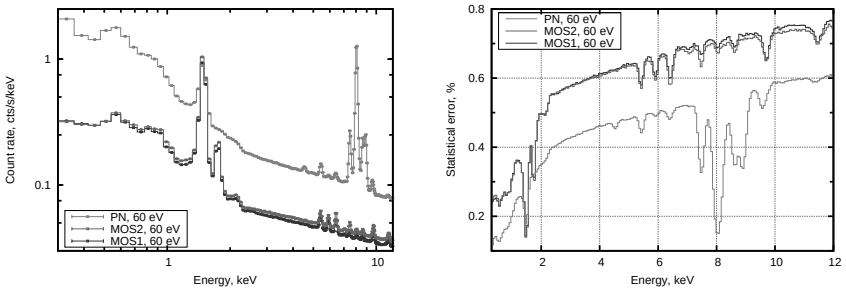

(a) Count rate per bin in each of the EPIC cameras (binned in 60 eV)

(b) Statistical relative error (defined as $1/\sqrt{\text{counts}}$) in each energy bin

Figure 5.13: Combined spectra for MOS1, MOS2 and PN cameras for our final dataset (see Table 5.5 for details). Strong instrumental lines are clearly visible in spectra of all cameras. Right panel shows the statistical relative error in each bin.

5.3 Spectral analysis of combined dataset

In this Section, we construct a model of co-added spectrum of all observations for each of the *XMM-Newton* EPIC cameras (MOS1, MOS2, PN) , using a simple `powerlaw` continuum model with a sum of several finite width `gaussians` in positions of bright instrumental lines (Sec. 5.3.2). The model is compiled in such a way that the large ($\gtrsim 2\sigma$) *negative* residuals are absent in the spectrum. The value of the systematic error is then estimated in Sec. 5.3.5. According to obtained value of systematic errors, we determine our criterium for line candidates. The total list of line candidates passing our criterium is then discussed, including comparison between different cameras and with closed-filter dataset 5.5.

5.3.1 An overview of existing approaches to study weak diffuse X-ray signals

The resulting spectrum of our combined dataset (with counts co-added by PI channels and then grouped to get 60 eV energy bins) is shown in Fig. 5.13. It has a shape, qualitatively similar to that of the blank sky dataset (cf. e.g. [327]): a continuum component plus a number of prominent lines. It is known that there are three major components of the “blank sky” spectrum — Galactic diffuse background, extragalactic diffuse background and instrumental (particle) background [325–327, 329] — and it is clear that our

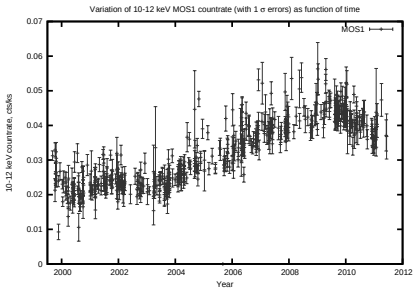

(a) Count rate for MOS1 camera in $\mathrm{counts/sec}$

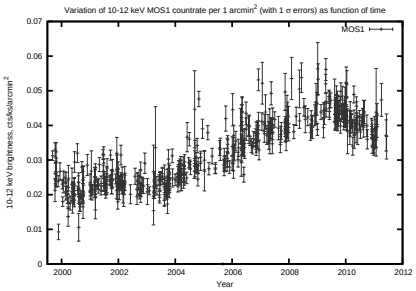

(b) Count rate per unit solid angle for MOS1 camera in $\mathrm{counts/sec/arcmin^2}$

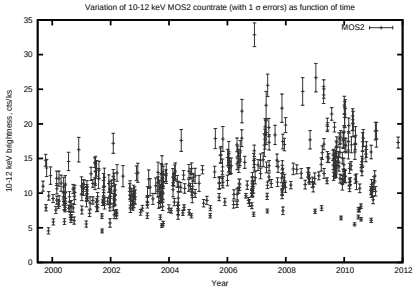

(c) Count rate for MOS2 camera in $\mathrm{counts/sec}$

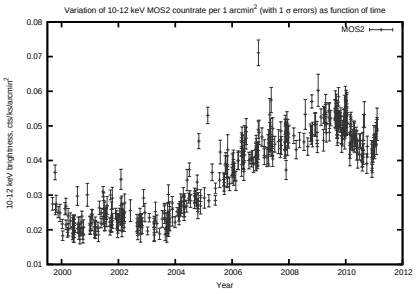

(d) Count rate per unit solid angle for MOS2 camera in $\mathrm{counts/sec/arcmin^2}$

Figure 5.14: Count rate at high energies (interval 10–12 keV,*MOS1 and MOS2 cameras*) in $\mathrm{counts/sec}$ (left panels) and in $\mathrm{counts/sec/arcmin^2}$ (right panels) as a function of revolution. Left panels may look like a random noise. However, in the panel (b) a clear long scale trend is visible. Notice that the same trend can be seen in both MOS1 and MOS2 cameras and therefore it is not related to the loss of the CCD6 by the MOS1 camera.

dataset has a similar structure. In particular, at energies below $\sim 1\,\mathrm{keV}$ the Galactic component dominates, while at energies above $\sim 2\,\mathrm{keV}$ the instrumental background becomes the dominant component.

Total cleaned exposure of the combined dataset that we have constructed is between 5.8 Ms (PN camera) and 8.7 Ms (MOS1 camera) (see Table 5.5). This large exposure (essentially two orders of magnitude longer than the exposure of a typical single *XMM-Newton* observation) means that the statistical errors in each energy bin are extremely small (between 0.1% and 0.8% for 60 eV binning, as Fig. 5.13b demonstrates). To extract meaningful bounds

from such large-exposure dataset one should be able to control systematics at a comparable level.[13]

Usually to study the diffuse signals, one subtracts from the raw spectra either "closed filter" background (i.e. particle-induced background) or "blank-sky" background (i.e. a combination of many observations without prominent sources and low level of diffuse emission). In our case neither of these approaches are applicable.

Indeed, the blank sky data would contain decaying dark matter line originating from the decays in the Milky Way halo. This fact has been explored before (see [223, 228, 358]) to put the limits on the lifetime of decaying dark matter. Subtracting such data would reduce all the advantages of a large dataset by removing a dominant component of the expected signal and lowering statistics (as the exposure of the latest blank-sky co-added observations is $\sim 2-4$ Ms [327]).

An alternative possibility would be to subtract a closed filter observation (as was done e.g. in [228] in search for decaying dark matter). However the exposure of available observations with closed filter is 1.20 Msec, 1.12 Msec, 0.78 Msec (for MOS1, MOS2, and PN cameras correspondingly).[14] As a result, the *subtraction* of rescaled closed filter data would mean ~ 3 times larger errorbars due to larger errors of the closed filter dataset. Moreover, the instrumental component of the *XMM-Newton* background is self-similar only on average, as we can see by comparing high-energy (10–12 keV) count rates of different observations (Fig. 5.14).

Finally, modeling of each individual observation (including ESAS model of instrumental background [329]) looks like a prohibitively challenging task for such a large number of independent observations. Namely, finding un-

[13]The level of systematics of the *XMM-Newton* is usually quoted at the level $5-10\%$. Indeed, according to Fig. 8 of the recent EPIC calibration report [339], the energy resolution has been degraded since the instrument launch for ~ 5 % (MOS) and ~ 10 % (PN) camera. According to [337], the flux ratios between different cameras do not change more than by 5 % with time (except 0.2-0.5 keV band, which is due to the known gradual degradation of MOS response matrices with time at these energies) which is the indication of relative stability of the ARF. Absolute effective area is now known with roughly 10 % precision, see [339]. In addition, a known problem with temporal and spatial variations of the MOS responses at energies below 0.5 keV has been fixed several years ago, see [245] for details. The emission of "standard candles" such as e.g. ζ Puppis [405] also remains constant at the level of 5-10%, which is also indication of the ARF stability from observation to observation.

[14]For PN camera we take a *combination* of Full Frame and Extended Full Frame modes as closed filter spectra are essentially the same in these two modes.

derlying spectral models for 399 observations (including parameters of the particle-induced instrumental background that are variable, as we discussed above) is extremely difficult. Moreover, fitting a thin Gaussian line simultaneously to all these observations would not be possible as the relative intensity of such a line is not known (due to the unknown dark matter content of different observed objects).

In this work we adopt a different approach, that allows us to find weak lines in the combined datasets at desired level. We develop a simple phenomenological model of the combined spectra. We then demonstrate that a weak line, present in all observations of the dataset can be successfully recovered at the expected level. Finally, we produce upper limits on flux of such a line from MOS and PN observations and discuss the origin of several candidate lines.

5.3.2 Constructing a spectral model of the combined dataset

For each EPIC camera the data can be described by a simple phenomenological model. A step-by-step construction procedure for individual cameras is discussed below in the Sections 5.3.3–5.3.4.

We model *count rates, normalized per energy bin*. Instead of using standard `RMF` and `ARF` response files we model them ourselves.[15] For each camera we model count rates by a simple `powerlaw` continuum model with a sum of several finite width `gaussians` modeling bright instrumental lines (see e.g. Table 5.6) for details). The resulting model possess the following properties:

1. The number of model free parameters is much smaller than the number of energy bins.
2. Residuals are distributed in such a way that roughly 68% of residuals are smaller than 1σ and roughly 95% of residuals are smaller than 2σ). However, the distribution of our residuals is deliberately skewed towards the increase of positive residuals (see below).
3. There are no significant *negative* residuals (at more than 2σ level in a single or adjacent 60 eV bins).
4. There are no broad *positive* residuals (several bins in a row), however, line-like residuals can remain.

[15] For MOS cameras we are using *diagonal RMF* matrices, relating bin numbers with energy as $E_i = 0.06 \times (N_{bin} - 0.5)$ since the width of the bin is 60 eV. For PN camera this turns out to be not enough for strong instrumental lines, see below Sec. 5.3.3.

Element	Energy (keV)	MOS	PN
K Kα	3.314	–	+
Ca Kα	3.692	–	+
Ti Kα	4.511	–	+
V Kα	4.952	–	+
Cr Kα	5.415	+	+
Mn Kα	5.899	+	+
Fe Kα	6.404	+	+
Fe Kβ	7.058	+	–
Ni Kα	7.478	+	+
Cu Kα	8.048	+	+
Zn Kα	8.639	+	+
Cu Kβ	8.905	–	+
Zn Kβ	9.572	–	+
Au Lα	9.713	+	+

Table 5.6: Known instrumental lines for the EPIC MOS and PN cameras in the energy range 2.5–10.8 keV, [329, 389, 406, 407]. The symbols + or – marks whether such a line has been previously detected in the spectrum of the corresponding camera. Some of these lines are actually several narrow lines from the same series with slightly different positions (for example, Kα_1 and Kα_2, see Table V of [408] for details), so we use the position of the strongest line (Kα_1 in our example). First three lines (K Kα, Ca Kα and V Kα) are detected by [389] by using special *calibration closed filter* background spectrum obtained by irradiating the instrument by ^{55}Fe radioactive calibration source. As a result, the intensities of the flourescent lines in calibration closed filter background are much higher compared to usual closed-filter background, so one can easily observe faint instrumental lines. The Fe Kβ line has been previously detected for MOS cameras only, see e.g. Fig. 2 of [329]. Our work find this line for PN camera, see Table 5.7 below (although with much lower significance compared to MOS cameras).

Finally, we lower the level of continuum to reduce the number of negative residuals (all of which then become less than 2σ). In this way we deliberately bias our procedure towards finding small line-like features in out combined dataset.

5.3.3 Constructing a spectral model for the PN combined dataset

In this Section, we describe a step-by-step procedure for constructing a phenomenological model for combined PN dataset binned by 60 eV. The procedure we use for constructing the model is the following

1. The spectrum of the PN camera is dominated by three strong instrumental lines at 8.045, 8.613 and 8.895 keV (with count rates exceeding $1\,\mathrm{cts/sec/cm^2}$, while the average level of continuum in the energy range 2.8–10.8 keV is at the level $0.1 - 0.3\,\mathrm{cts/sec/cm^2}$). Therefore, we start by excluding the 7.56–9.30 keV energy range (this energy range is also excluded from the final restrictions based on PN spectrum extremely low sensitivity). Due to extremely high statistics, the deviations of the shapes of these lines from purely Gaussian form is very large compared to statistical error and therefore they are difficult to model properly. On the other hand, these residuals are not typical for the whole spectrum, so we do not treat them as a systematic error.
2. We use the energy ranges free from the prominent emission lines (2.70–4.35 and 10.05–11.1 keV) to determine parameters of the `power law` continuum component, see Fig. 5.15 for details.
3. We add instrumental lines with the known positions (see Table 5.6) to the `powerlaw` continuum model, with *fixed* parameters, determine line dispersions and normalizations using best-fit procedure. The results is shown in Fig. 5.16a.
4. We compensate two evident line-like residuals by adding two line candidates at 5.0 and 7.075 keV. The fit quality becomes somewhat better, see Fig. 5.16b for details. The significance of these lines is 7.8σ (for 5.0 keV line) and 3.6σ for 7.075 keV line.[16]
5. At this stage we see that there are systematically positive residuals in many consecutive bins, adjacent (left) to the instrumental lines. We assume this extra continuum to be non-Gaussian tails strong instrumental lines at energies. To demonstrate this we generate (using `fakeit` command of `Xspec` three instrumental lines at positions 6.42, 7.456 and 8.045 keV. We use response matrices (`RMF`) of actual PN observations to reconstruct the correct non-Gaussian shape of the lines.

[16] Significance of these lines is defined as $\sqrt{\Delta\chi^2}$ when adding 1 extra degree of freedom (line normalization) to the fit model.

The result is shown in Figs. 5.17. Each of these lines is well described as

$$F(E) = n_1 \times e^{-\frac{(E-E_1)^2}{2\sigma_1^2}} + n_2 \times e^{-\frac{(E-E_2)^2}{2\sigma_2^2}} + n_{\rm br} F_{\rm br}(E), \qquad (5.2)$$

where $F_{\rm br}(E) = (E/E_{\rm br})^{\alpha_{\rm low}}$ at $E < E_{\rm br}$ and $F_{\rm br}(E) = (E/E_{\rm br})^{\alpha_{\rm high}}$ at $E \geq E_{\rm br}$. The model contains 10 parameters.

6. Next we try to model continuum excess at 5–6 keV (see Fig. 5.16b for details) as a low-energy tail of the non-Gaussian shaped (5.2) of strong instrumental lines at 6.4, 7.5 and 8.0 keV. The results of the modeling are shown in Fig. 5.17. The details of narrow line simulation are described in Sec. 8.4.3. The results are shown in Fig. 5.18.
7. As we can see from Fig. 5.18, extra continuum from instrumental lines is *not* enough to model the 5-6 keV spectrum continuum. The fit can be significantly improved by allowing normalizations of different components in Eq. 5.2 to vary. This results in 6 extra parameters (2 extra normalizations for each of three modeled instrumental lines) but allowing them to very improves the fit quality very significantly. Fig. 5.20 shows that resulting best-fit continuum for instrumental lines is about an order of magnitude higher than in Fig. 5.17.
8. The resulting fit is shown in Fig. 5.19. Now, fit quality becomes much more reasonable than in previous fits, so we improve the residual local excesses by rebinning nearby bins. The goal is to remove all local negative residuals at the level higher than 2σ.[17] For 4.5 and 5.4 keV lines, we rebinned central 3 bins (180 eV) such that central bin has now 120 eV, and off-center – 30 eV each. We have not done it for 9.6 keV bump because it is known that there are two close instrumental line. For 3.12 – 3.24, 3.24 – 3.36, 3.36 – 3.48, 3.54 – 3.66, 3.78 – 3.90, 3.96 – 4.08, 6.00 – 6.12, 6.48 – 6.60, 9.72 – 9.84, 9.84 – 9.96, 9.96 – 10.08 keV we combine adjacent 60 eV bins to produce single 120 eV bins. Similarly, we combine bins in 5.49 – 5.64 keV in a single 150 eV bin.
9. For additional increase of negative residuals, we use slightly (0.5 %) smaller normalization of powerlaw continuum. The powerlaw index remains the same. Such renormalization allows us to obtain more conservative constraints for normalization of the narrow line candidates.

[17] This is done because our goal is not construct the best fit model of the underlying dataset, but to optimize the model that would not "hide" weak residual lines.

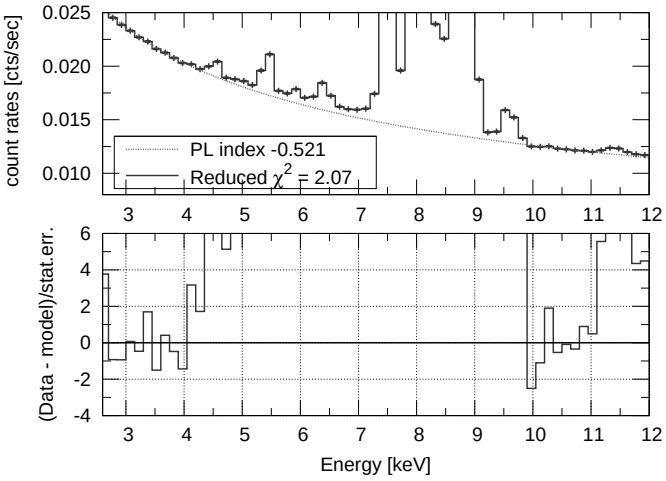

Figure 5.15: Conservative continuum powerlaw model for PN spectrum binned by 150 eV obtained by fitting at 2.70–4.35 and 10.05–11.1 keV energy ranges which are free from lines. Significant positive residuals are clearly visible in the positions of the instrumental lines.

The obtained best-fit reference model is shown in Fig. 5.21. It is reasonable as the number of free parameters (16) is much smaller than the number (92) of the energy bins.

5.3.4 Constructing a spectral models for MOS combined datasets

Best-fit reference models for MOS1 and MOS2 cameras are built in the same way as for PN camera, see Sec. 5.3.2. The major difference is that we cannot adequately fit the continuum with a single `powerlaw` and thus produced a combination of two `powerlaw` models with different indices and normalizations at $\lesssim 5$ keV and $\gtrsim 6$ keV energies. The transition between these two powerlaw models is modeled with a step function at ~ 5.4 keV. Due to relative weakness of MOS instrumental lines (compared to PN camera) we model all instrumental lines with the help of pure `gaussian` model.

The resulting fit is shown in Fig. 5.22.

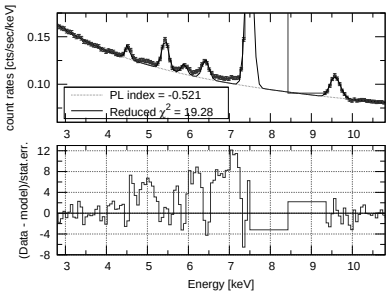

(a) Adding several gaussians to powerlaw model from Fig. 5.15 corresponding to *bright instrumental lines*. Their positions are fixed according to Table 5.6, but dispersion and normalizations are determined via χ^2 fitting procedure.

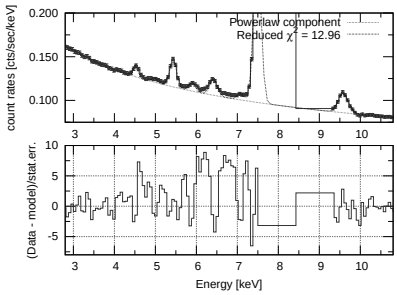

(b) The same as in Fig. 5.16a, but with two extra gaussian at 5.0 and 7.075 keV corresponding to *line candidates*. The fit quality is now significantly better though there are still some residuals at 6.7-7.0 keV.

Figure 5.16: Accounting for the line-like residuals in the model of the combined PN spectrum. In Fig. 5.16a, we add to the `powerlaw` model (shown as pink dotted line) several `gaussians` in the positions of well-established *instrumental lines* (Table 5.6). Energy range 7.56-9.30 keV around three most prominent instrumental lines (8.045, 8.613 and 8.895 keV) is not used in this modeling. Significant decrease of line residuals compared to previous Fig. 5.15 is shown. In Fig. 5.16b, we add two extra gaussians corresponding to *line candidates* at 5.0 and 7.075 keV. In both figures, 3σ error bars are shown for convenience.

5.3.5 Estimating systematic errors

According to Figs. 5.21 and 5.22, the fit quality is statistically unacceptable. The fact that reduced χ^2 is significantly larger than 1 means that the average residuals are systematically larger compared to statistically acceptable fit. For such a fit, we expect 68% of all residuals have absolute values smaller than 1σ, 95% – smaller than 2σ. In reality, for PN camera 68% of all residuals have absolute values larger than 0.81 statistical errors, 95% of residuals – larger than 2.20 statistical errors, so the average residual value is estimated as $(0.81 + 2.20/2)/2 = 0.96$ (in units of statistical errors). Because the fit of PN data have used 90 energy bins, and the model has 18 free parameters, the expected average value of residual is only $1 - 18/90 = 0.80$ (in units of statistical errors). To increase the average residual from 0.80 to 0.96 statistical error, we need to add some systematical error in quadratures. The necessary value of systematic error should be $\sqrt{0.96^2 - 0.80^2} = 0.53$ (in units

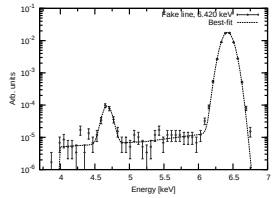

(a) Shape of strong instrumental line at 6.420 keV.

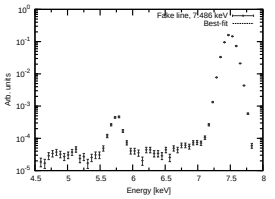

(b) Shape of strong instrumental line at 7.456 keV.

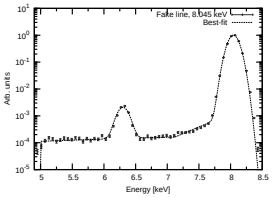

(c) Shape of strong instrumental line at 8.045 keV.

Figure 5.17: Determining (non-Gaussian) shapes of strong instrumental lines for the PN camera. Using `fakeit` procedure from `Xspec` and actual response matrices of the EPIC PN camera, we modeled long exposure observation of instrumental lines at positions 6.420, 7.456 and 8.045 keV. Line normalizations are shown in arbitrary units (*the units are same across all panels*, i.e. the leftmost line is the weakest and the rightmost line is the strongest). Clearly seen are second Gaussian peaks and low-energy continuum tails. Error bars are statistical, green solid lines are best fit models (using Eq. (5.2)). Each line is described by 10 parameters (instead of 3 in the Gaussian case).

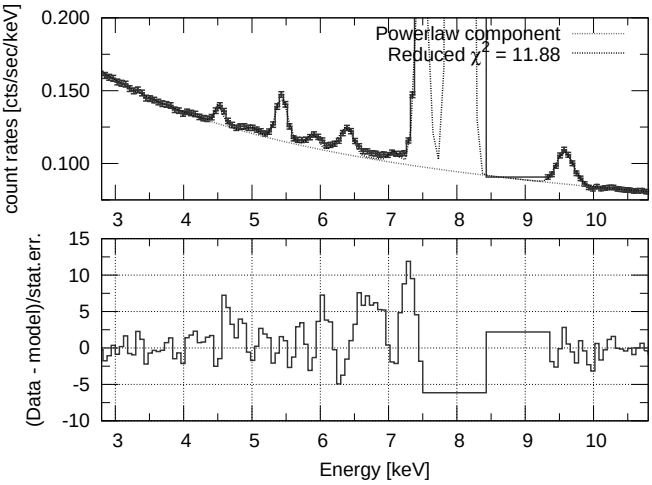

Figure 5.18: The same as in Fig. 5.16b but with modification of three instrumental lines at 6.420, 7.456 and 8.045 keV according to their modeling in Fig. 5.17. In this figure, 3σ error bars are shown for convenience.

of statistical errors), or (by assuming mean statistical error for PN camera equal to 0.48%), $0.53 \times 0.48 = 0.25\%$ (in absolute value). Similar calculations

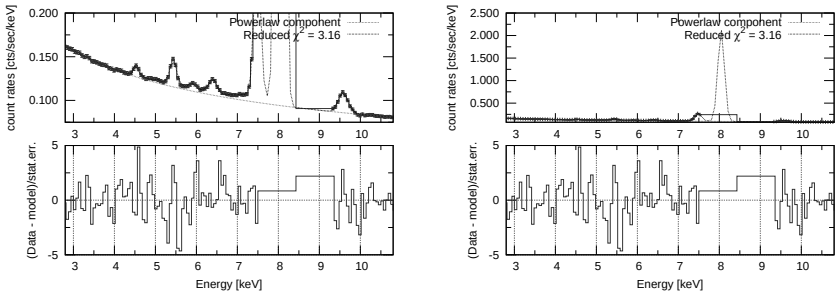

(a) The same as in Fig. 5.18 but now the relative contribution of primary gaussian, continuum and secondary gaussian is not fixed and determined from the least-squares method.

(b) The same as is Fig. 5.19a but scaled for better visualization of high-energy line.

Figure 5.19: PN spectra modeled with fake gaussians at 6.420, 7.456 and 8.045 keV. Compared to Fig. 5.18, now the relative contribution of primary gaussian, continuum and secondary gaussian is not fixed and determined from the least-squares method. The resulting fit quality is much better than for our previous attempt, see Fig. 5.18 for details. In both figures, 3σ error bars are shown for convenience.

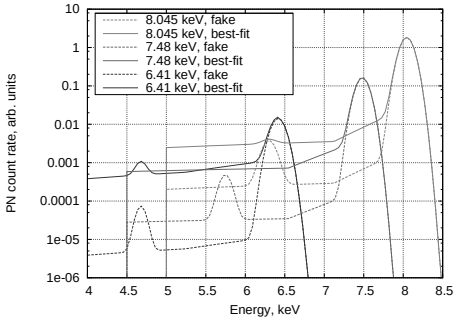

Figure 5.20: Comparison of the best-fit fake Gaussian models (solid) used in previous Fig. 5.19 with initial fake Gaussian models from Fig. 5.17 (dashed), see Eq. (5.2).

of absolute value for systematic errors for MOS1 and MOS2 camera give 0.19% and 0.41%, respectively.

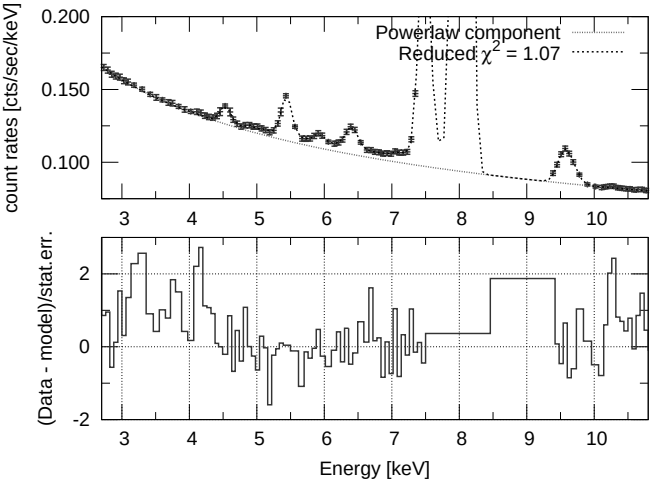

Figure 5.21: Resulting fit of PN combined dataset (see text). Most of the bins have 60 eV width, some of bins have been rebinned by 30, 120 and 150 eV in order to decrease the narrow negative residuals. To further reduce the negative residuals, we decreased the normalization of the powerlaw continuum by 0.5%. *For better error visualisation, 3σ error bars are shown*.

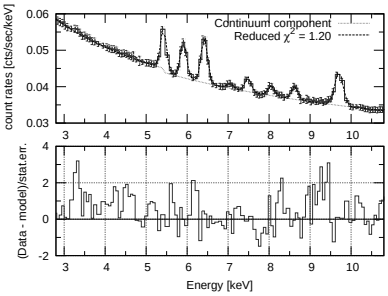

(a) Modeling total (2.8-10.8 keV) spectra for continuum model (consisting of two powerlaws connected with a step function) plus several gaussian lines. Similar to modeling of PN spectrum shown in Fig. 5.21, we decrease the normalization of MOS continuum by 0.5%. For better error visualisation, 3σ error bars are shown.

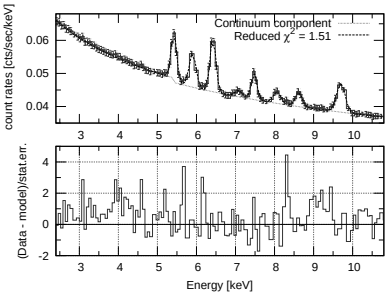

(b) The same as in the left part but for MOS2 camera.

Figure 5.22: Modeling of MOS1 and MOS2 count rates at 2.8-10.8 keV.

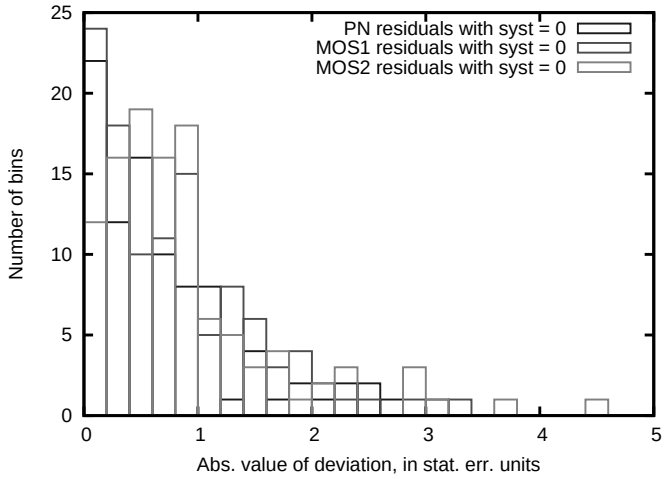

Figure 5.23: Distribution of residuals for MOS (Fig. 5.22, upper panels) and PN (Fig. 5.21, upper panel) cameras in the final dataset. The distribution is slightly non-Gaussian, especially due to presence of several large residuals. By adding a systematic error (0.19% for MOS1, 0.41% for MOS2 and 0.21% for PN camera) in quadratures we increase total error so the distribution (in units of total errors) becomes close to Gaussian, see Sec. 5.3.5 for calculation details.

5.4 Detection of faint lines

To search for faint narrow lines, we use the reference models (described in details in Sec. 5.3.2 and 5.3.4) shown in Figs 5.21 and 5.22. The extra Gaussian line with fixed position and small dispersion is added to our reference model in some particular energy bin. We specify the line's dispersion as fixed function of energy, defined by the central values (see the left panel Fig. 5.24, see Section 5.4.1.1 for details). To account for possible negative residuals, we allow the normalization of the extra line to be negative. Then, by using least-squares fitting procedure, we define the best-fit value of the normalization of the extra line (allowing all other model parameters, except position and dispersion of the extra line to vary). By changing line position in 10 eV increments (much smaller than the energy resolution of the instrument) this procedure is repeated for the energy ranges of our interest (2.8-10.8 keV).

5.4.1 Verification of line detection procedure.

Due the presence of various sources of systematic error, it is crucial to perform extensive tests checking validity of our procedure of line detection. Namely, by adding faint narrow line with certain intensity our procedure of line detection should detect this line at a given position and intensity (within the confidence ranges).

5.4.1.1 Simulations of narrow lines.

We simulate a narrow `gaussian` line (with $\sigma_E = 0.001$ keV) for each observation combining it with appropriate RMF and ARF constructed with `rmfgen` and `arfgen`, respectively. We use the same value of initial line normalization for each camera. The simulations were performed with the `fakeit` command, a part of `Xspec` spectral fitting package [409]. Then, the simulated spectra were combined together for each camera (MOS1, MOS2, PN) and modeled with the help of `gaussian` model having 2 free parameters: energy dispersion σ and fraction F of counts contributing to `gaussian`,

$$f(E) = \frac{F \times N_{counts}}{\sqrt{2\pi\sigma^2}} \exp\left(-\frac{(E-E_0)^2}{2\sigma^2}\right). \tag{5.3}$$

The central energy E_0 was kept fixed to the initial central energy of the line.

The results are shown in Fig. 5.24. As we expect, $F \lesssim 1$. The obtained values of σ correspond to $\Delta E \simeq 100 - 200$ eV, consistent with values known from literature[18], see e.g. Figs 25-26 of [320].

To calculate intensity of the recovered line, one should divide the obtained countrate (in cts/s) by the effective area of the corresponding instrument. To calculate the effective area, we used the following procedure. For each observation, we used the actual effective area (binned by 5 eV bins) produced by `arfgen` procedure. Then, for each energy bin we calculate the exposure and FoV-weighted mean for each observation. Finally, to account the finite energy resolution of the cameras (with FWHM = 100-200 eV depending on energy, see e.g. left Fig. 5.24 for details), we rebin the obtained effective area by 150 eV bins. The results are shown in Fig. 5.12.

[18] Note that $\Delta E \equiv 2\sigma\sqrt{2\log(2)} \simeq 2.35\sigma$, according to definition of FWHM.

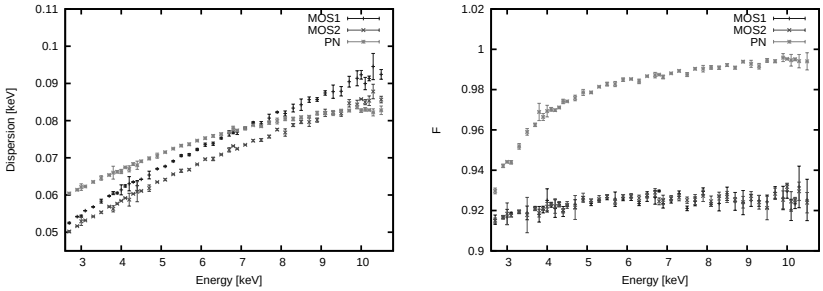

Figure 5.24: *Left*: Dispersion σ_E of a narrow line with energy E (note that FWHM for a Gaussian line is $2.35 \times \sigma_E$). The internal dispersion of the line is 1 eV. *Right*: Fraction F of a photons contributing to narrow gaussian with dispersion σ_E (see left Figure).

5.5 Results

5.5.1 Identifying lines

The procedure, described in Section 5.4 led to identification of a number of line-like residuals in our datasets.

The properties of instrumental lines identified with our procedure are shown in Table 5.7.

5.5.2 Upper limits on the flux in narrow line

The 3σ upper bounds on intensities of extra narrow lines (per unit solid angle) are presented in Fig. 5.26. To obtain these bounds, we used "statistical" method described e.g. in [46]. Namely, we add a narrow line at fixed energy to combined dataset. The value of line dispersion is fixed equal to its expectation, see Fig. 5.24 for details. Then, we calculate the intensity which increases total χ^2 by 3^2 (which corresponds to 3σ bound). To calculate the values of χ^2 we add systematical errors obtained in Sec. 5.3.5. The "gaps" on the upper bounds are due to strong instrumental lines. To account possible uncertainties on line determination, see Fig. 5.25 for details, we weaken our bounds by multiplying the limiting intensities by 1.05 and 1.3 for energies below and above 5.3 keV, respectively. For comparison, we show corresponding bounds obtained from central part of Andromeda galaxy, see Fig. 8 of [230] for details. From Eq. 4.1 we expect the increase of sensitivity

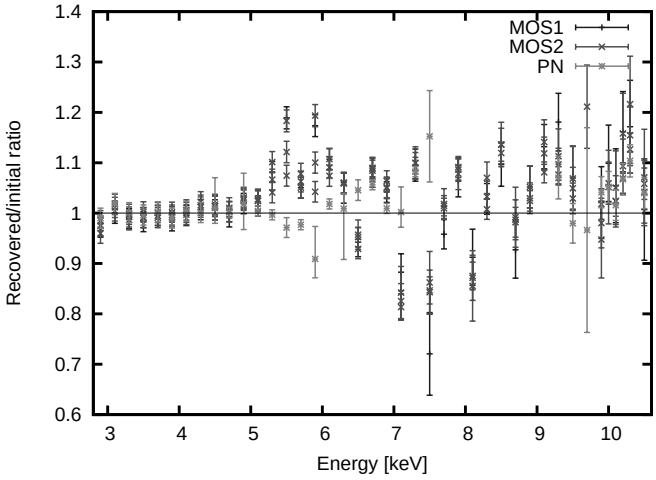

Figure 5.25: Ratios between intensities of initial and recovered lines, together with 1σ errors. Below ~ 5.3 keV, the ratio deviates from 1 within 5%, above ~ 5.3 keV – within 30%. As a result, in Fig. 5.26 we weaken our bounds by multiplying the limiting intensities by additional factors 1.05 and 1.3, respectively.

equal to ratios of $\sqrt{t_{exp} \times \Omega_{\rm fov}}$, or $\sim$8.7, $\sim$8.7 and $\sim$6.3 for MOS1, MOS2 and PN cameras, respectively. Indeed, as we see from Fig. 5.26, such an improvement is close to observed one at $\lesssim 5$ keV. At larger energies, the improvement is significantly smaller, due to contribution from strong instrumental lines.

To check the validity of our bounds presented in Fig. 5.26, we use the following procedure. After adding a simulated narrow line with fixed intensity to our combined dataset, see Sec. 5.4.1 for details, we try to detect the simulated line in a obtained spectrum. The results for PN camera are shown in Fig. 5.27. The lines detected at $\geq 3\sigma$ level and not detected are marked by the crosses and multiplication signs, respectively. As we expected, all crosses are located below the bounds. This means that are procedure does not produce any "spurious" line candidates, and the obtained bounds are very conservative.

Finally, we produce new bounds on sterile neutrino dark matter parameters – mass of dark matter particle $M_{\rm DM}$ and mixing angle $\sin^2(2\theta)$. To do that, we first calculate the expected dark matter signal. Milky Way contribution is estimated using the conservative dark matter profile from [372], see Table 5.1 and Fig. 5.1 for details. This gives the exposure-weighted mean

MOS1 (keV/ cts/sec/cm^2/ is known?)	MOS2 (keV/ cts/sec/cm^2/ is known?)	PN (keV/ cts/sec/cm^2/ is known?)	Possible line (keV)
—/—/—	—/—/—	4.532/5.2×10^{-6}/+	4.511 (Ti Kα)
—/—/—	—/—/—	4.917/1.4×10^{-6}/+	4.952 (V Kα)
5.428/1.6×10^{-5}/+	5.426/1.7×10^{-5}/+	5.439/1.3×10^{-5}/+	5.415 (Cr Kα)
5.910/1.8×10^{-5}/+	5.901/1.8×10^{-5}/+	5.927/2.7×10^{-6}/+	5.899 (Mn Kα)
6.419/2.8×10^{-5}/+	6.422/3.1×10^{-5}/+	6.420/9.2×10^{-6}/+	6.404 (Fe Kα)
7.052/4.2×10^{-6}/+	7.079/7.1×10^{-6}/+	7.091/9.0×10^{-7}/–	7.058 (Fe Kβ)
7.484/1.6×10^{-5}/+	7.477/2.7×10^{-5}/+	7.486/1.5×10^{-4}/+	7.478 (Ni Kα)
8.054/1.9×10^{-5}/+	8.066/2.5×10^{-5}/+	8.045/2.1×10^{-3}/+	8.048 (Cu Kα)
8.623/3.7×10^{-5}/+	8.619/4.1×10^{-5}/+	8.626/2.2×10^{-4}/+	8.639 (Zn Kα)
—/—/—	—/—/—	8.904/2.8×10^{-4}/+	8.905 (Cu Kβ)
—/—/—	—/—/—	9.553/5.2×10^{-5}/+	9.572 (Zn Kβ)
9.703/2.5×10^{-4}/+	9.701/2.1×10^{-4}/+	9.698/2.0×10^{-5}/+	9.713 (Au Lα)

Table 5.7: Parameters of instrumental lines for the EPIC MOS and PN cameras identified with our procedure (first 3 columns). Each column shows: **(i)** *energy of detected line* [keV] / **(ii)** *intensity of detected line* [cts/sec/cm^2] / **(iii)** whether the line has been previously known as an instrumental one (sign "+" or "–") for the corresponding camera. For PN line at ~ 4.95 keV, the corresponding V Kα instrumental line has been observed in the mode with significantly enhanced intensity of instrumental lines (the *CalClosed* mode), see [389] for details. The initial energies of fluorescence lines are taken from Table V of [408], similar to previous Table 5.6. We do not put here K Kα and Ca Kα lines because they are not detected in our datasets. All line positions are reconstructed with precision ≤ 40 eV, much better that the energy resolution of EPIC cameras.

column density 130 $\mathrm{M}_\odot/\mathrm{pc}^2$. We also added exposure-weighted contribution from Andromeda galaxy using the most conservative profile of [11], see Fig. 5.2. Because M31 exposure is only $\sim 1/5$ of total, the corresponding column density contribution from M31 is about 20 $\mathrm{M}_\odot/\mathrm{pc}^2$. To be conservative, we did not add contribution from other galaxies. This gives us the total exposure-weighted mean column density for our combined dataset equal to 150 $\mathrm{M}_\odot/\mathrm{pc}^2$.

The resulting bounds on sterile neutrino parameters obtained from combination of all 3 cameras are shown in Fig. 5.28. We strenghen previous

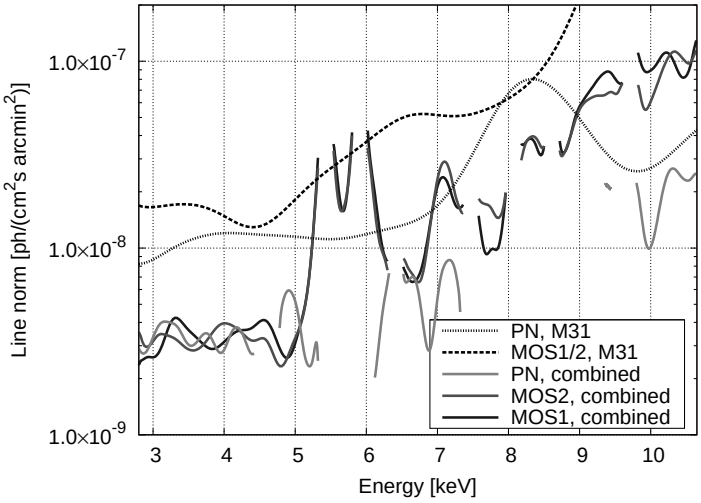

Figure 5.26: 3σ upper bounds on intensities (per unit solid angle) of a narrow line (grey solid lines). The parameter space *above* the lines is excluded. The errorbars are discussed in Sec. 5.3.5. To account possible uncertainties on line determination, see Fig. 5.25 for details, we weaken our bounds by multiplying the limiting intensities by 1.05 and 1.3 for energies below and above 5.3 keV, respectively. For comparison, we show smoothed bounds for MOS1/MOS2 and PN cameras from Fig. 8 of [230]. Due to larger statistics of our dataset, we expect the improvement of our bounds with respect to M31 by about 8.7 (for MOS cameras) and about 6.3 for PN camera. The gaps are at the positions of strong instrumental lines, where the sensitivity of our method is low.

X-ray bounds (shaded region in the upper right corner on Fig. 5.28) above $\sim$5.5 keV (excluding several energy ranges dominated by instrumental lines) up to a factor 5-6. This is possible due to large (for a factor of ~ 50) increase of exposure for our combined dataset, and the specially method of data analysis allowing to control systematic errors at the sub-% level (i.e. close to statistical errors).

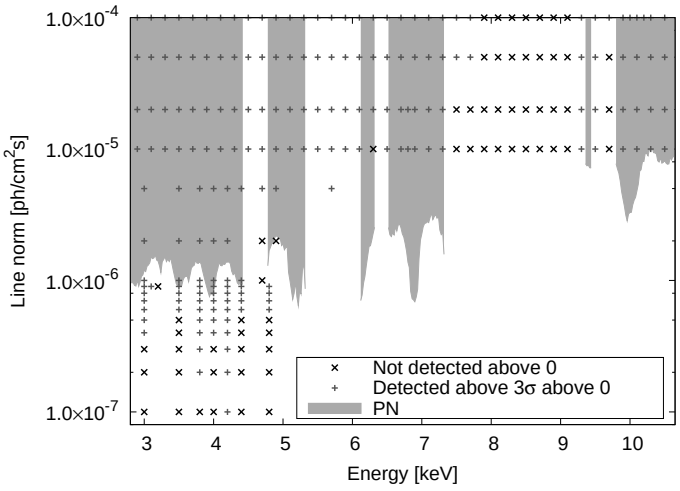

Figure 5.27: Verification of the sensitivity of our method. To check the reliability of the bounds of Fig. 5.26, we add to the PN combined dataset simulated lines with central energies and normalizations and check whether these lines are detected at $\geq 3\sigma$ level. During the simulations, the statistical fluctuations of number of counts are taken into account. Those lines that are detected at $\geq 3\sigma$ level are marked by the crosses, those are not – by multiplication signs. The correct bounds should have crosses inside the shaded area and, more importantly, multiplication signs outside the shaded region. This is what one indeed sees in this Figure. The fact that in most cases crosses continue to be detected below the shaded area means that our bounds are very conservative.

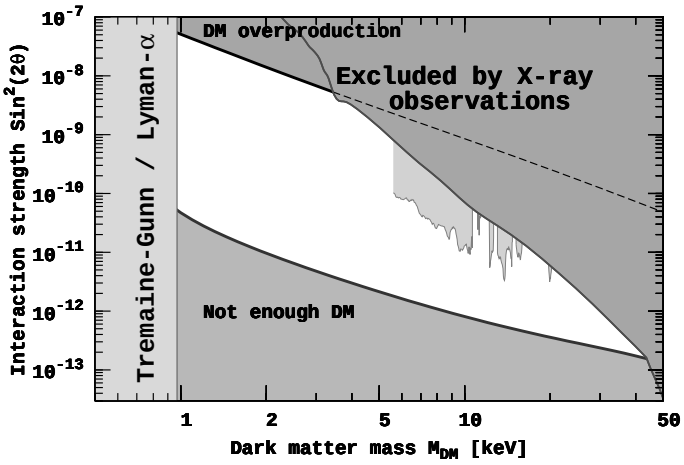

Figure 5.28: The allowed region of parameters of sterile neutrino dark matter in the νMSM (white unshaded region) confronted with existing and projected experimental bounds. For any combination of mass and mixing angle between two black curves the necessary amount of dark matter can be produced (given the presence of certain amount of lepton asymmetry in the plasma, generated by two other sterile neutrinos). The shaded region in the upper right corner is excluded by the non-observation of decaying dark matter line in X-rays [221, 223–225, 228, 230, 231, 318, 357, 358]. Grey regions between $\sim 5\,\mathrm{keV}$ and $\sim 20\,\mathrm{keV}$ are excluded from analysis of combined dataset described in this thesis (Chapter 5). The gaps are due to the presence of strong instrumental lines at certain energies (where the combination method does not provide any improvement over earlier bounds). The lower limit of $\sim 5\,\mathrm{keV}$ is due to the presence of instrumental lines and absorption edge at energies $1 - 2.5\,\mathrm{keV}$ and emission of the Milky Way, dominating at lower energies. In the region below $1\,\mathrm{keV}$ sterile neutrino dark matter is 'too light' and is ruled out based on 'Tremaine-Gunn' like arguments [46] and on the Lyman-α analysis [99, 131].